also in two dimensions. Realization of the paradigmatic quantum phase transition from such an artificial valence bond solid to a Heisenberg antiferromagnet (*41*) therefore seems within reach of present experiments.

Recently, we became aware of similar experimental results in two dimensions (*42*, *43*).

REFERENCES AND NOTES

1. P. W. Anderson, *Science* **235**, 1196–1198 (1987).
2. K. L. Hur, T. M. Rice, *Ann. Phys.* **324**, 1452–1515 (2009).
3. A. Auerbach, *Interacting Electrons and Quantum Magnetism* (Springer Science & Business Media, 1994).
4. T. Giamarchi, *Quantum Physics in One Dimension* (Clarendon, 2004).
5. T. Esslinger, *Ann. Rev. Condens. Matter Phys.* **1**, 129–152 (2010).
6. R. Jördens, N. Strohmaier, K. Günter, H. Moritz, T. Esslinger, *Nature* **455**, 204–207 (2008).
7. U. Schneider *et al.*, *Science* **322**, 1520–1525 (2008).
8. R. Jördens *et al.*, *Phys. Rev. Lett.* **104**, 180401 (2010).
9. S. Taie, R. Yamazaki, S. Sugawa, Y. Takahashi, *Nat. Phys.* **8**, 825–830 (2012).
10. P. M. Duarte *et al.*, *Phys. Rev. Lett.* **114**, 070403 (2015).
11. D. Greif *et al.*, *Science* **351**, 953–957 (2016).
12. L. W. Cheuk *et al.*, *Phys. Rev. Lett.* **116**, 235301 (2016).
13. C. Hofrichter *et al.*, *Phys. Rev. X* **6**, 021030 (2016).
14. E. Cocchi *et al.*, *Phys. Rev. Lett.* **116**, 175301 (2016).
15. S. Trotzky, Y.-A. Chen, U. Schnorrberger, P. Cheinet, I. Bloch, *Phys. Rev. Lett.* **105**, 265303 (2010).
16. D. Greif, T. Uehlinger, G. Jotzu, L. Tarruell, T. Esslinger, *Science* **340**, 1307–1310 (2013).
17. D. Greif, G. Jotzu, M. Messer, R. Desbuquois, T. Esslinger, *Phys. Rev. Lett.* **115**, 260401 (2015).
18. R. A. Hart *et al.*, *Nature* **519**, 211–214 (2015).
19. S. Murmann *et al.*, *Phys. Rev. Lett.* **115**, 215301 (2015).
20. L. W. Cheuk *et al.*, *Phys. Rev. Lett.* **114**, 193001 (2015).
21. M. F. Parsons *et al.*, *Phys. Rev. Lett.* **114**, 213002 (2015).
22. E. Haller *et al.*, *Nat. Phys.* **11**, 738–742 (2015).
23. G. J. A. Edge *et al.*, *Phys. Rev. A* **92**, 063406 (2015).
24. A. Omran *et al.*, *Phys. Rev. Lett.* **115**, 263001 (2015).
25. G. Zürn *et al.*, *Phys. Rev. Lett.* **110**, 135301 (2013).
26. J. Sirker, A. Klümper, *Phys. Rev. B* **66**, 245102 (2002).
27. E. V. Gorelik *et al.*, *Phys. Rev. A* **85**, 061602 (2012).
28. B. Sciolla *et al.*, *Phys. Rev. A* **88**, 063629 (2013).
29. F. H. L. Essler, H. Frahm, F. Göhmann, A. Klümper, V. E. Korepin, *The One-Dimensional Hubbard Model* (Cambridge Univ. Press, 2005).
30. Supplementary text available as supplementary materials on *Science* Online.
31. J. Sebby-Strabley, M. Anderlini, P. Jessen, J. Porto, *Phys. Rev. A* **73**, 033605 (2006).
32. S. Fölling *et al.*, *Nature* **448**, 1029–1032 (2007).
33. F. Werner, O. Parcollet, A. Georges, S. R. Hassan, *Phys. Rev. Lett.* **95**, 056401 (2005).
34. R. Olf, F. Fang, G. E. Marti, A. MacRae, D. M. Stamper-Kurn, *Nat. Phys.* **11**, 720–723 (2015).
35. J.-S. Bernier *et al.*, *Phys. Rev. A* **79**, 061601 (2009).
36. T.-L. Ho, Q. Zhou, *Proc. Natl. Acad. Sci. U.S.A.* **106**, 6916–6920 (2009).
37. A. M. Rey *et al.*, *Europhys. Lett.* **87**, 60001 (2009).
38. S. Trebst, U. Schollwöck, M. Troyer, P. Zoller, *Phys. Rev. Lett.* **96**, 250402 (2006).
39. S. Nascimbène *et al.*, *Phys. Rev. Lett.* **108**, 205301 (2012).
40. M. Lubasch, V. Murg, U. Schneider, J. I. Cirac, M.-C. Bañuls, *Phys. Rev. Lett.* **107**, 165301 (2011).
41. T. Senthil, A. Vishwanath, L. Balents, S. Sachdev, M. P. A. Fisher, *Science* **303**, 1490–1494 (2004).
42. M. F. Parsons *et al.*, *Science* **353**, 1253–1256 (2016).
43. L. W. Cheuk *et al.*, *Science* **353**, 1260–1264 (2016).

QUANTUM SIMULATION

Observation of spatial charge and spin correlations in the 2D Fermi-Hubbard model

Lawrence W. Cheuk,[1]* Matthew A. Nichols,[1]* Katherine R. Lawrence,[1] Melih Okan,[1] Hao Zhang,[1] Ehsan Khatami,[2] Nandini Trivedi,[3] Thereza Paiva,[4] Marcos Rigol,[5] Martin W. Zwierlein[1]†

Strong electron correlations lie at the origin of high-temperature superconductivity. Its essence is believed to be captured by the Fermi-Hubbard model of repulsively interacting fermions on a lattice. Here we report on the site-resolved observation of charge and spin correlations in the two-dimensional (2D) Fermi-Hubbard model realized with ultracold atoms. Antiferromagnetic spin correlations are maximal at half-filling and weaken monotonically upon doping. At large doping, nearest-neighbor correlations between singly charged sites are negative, revealing the formation of a correlation hole, the suppressed probability of finding two fermions near each other. As the doping is reduced, the correlations become positive, signaling strong bunching of doublons and holes, in agreement with numerical calculations. The dynamics of the doublon-hole correlations should play an important role for transport in the Fermi-Hubbard model.

A central question in the study of cuprate high-temperature superconductors is how spin and charge correlations give rise to the wealth of observed phenomena. Antiferromagnetic order present in the absence of doping quickly gives way to superconductivity upon doping with holes or electrons (*1*), suggesting the viewpoint of competing phases. On the other hand, antiferromagnetic correlations can also occur in the form of singlet bonds between neighboring sites. In fact, it has been proposed (*2*) that superconductivity could result, upon doping a Mott insulator, from the condensation of such resonating valence bonds. It has also been argued (*1*) that the pseudogap and "strange metal" regions are supported by a liquid of spin-singlets. This argument has spurred the simultaneous examination of nearest-neighbor spin and charge correlations, which might reveal the underlying mechanisms of pairing and transport.

In recent years, ultracold atomic gases have been established as pristine quantum simulators of strongly correlated many-body systems (*3–5*). The Fermi-Hubbard model is of special importance, thanks to its paradigmatic role for the study of high–critical temperature cuprates. At low temperatures and away from half-filling, solving the Fermi-Hubbard model theoretically is very challenging because of the fermion sign problem. Central properties of Fermi-Hubbard physics—from the reduction of double occupancy (*6*, *7*) and of compressibility (*8*, *9*) as the repulsion is increased, to short-range antiferromagnetic correlations (*10–12*) and the equation of state (*9*, *13*, *14*)—have been observed in ultracold atom experiments. The recently developed Fermi gas microscopes (*13*, *15–19*) have led to the direct observation of two-dimensional (2D) fermionic Mott insulators, band insulators, and metals with single-atom, single-site–resolved detection (*20*, *21*). The strength of this technique, however, is on full display when single-site detection is used to directly measure correlations in the gas, as has been achieved with bosons (*22–24*).

[1]Department of Physics, MIT-Harvard Center for Ultracold Atoms, and Research Laboratory of Electronics, Massachusetts Institute of Technology (MIT), Cambridge, MA 02139, USA. [2]Department of Physics and Astronomy, San José State University, San José, CA 95192, USA. [3]Department of Physics, The Ohio State University, Columbus, OH 43210, USA. [4]Instituto de Fisica, Universidade Federal do Rio de Janeiro, Caixa Postal 68.528, 21941-972 Rio de Janeiro, RJ, Brazil. [5]Department of Physics, The Pennsylvania State University, University Park, PA 16802, USA.
*These authors contributed equally to this work. †Corresponding author. Email: zwierlein@mit.edu

In our study, we used a Fermi gas microscope of ^{40}K atoms to directly observe charge and spin correlations in the 2D Fermi-Hubbard model (15, 21). Spin correlations displaying antiferromagnetic behavior have also been observed very recently with fermionic ^{6}Li in one (25) and two (26) dimensions. We employ the local resolution to simultaneously obtain correlations in the entire range from zero doping (half-filling) to full doping (zero filling), as the density varies in the underlying trapping potential. The microscope measures the parity-projected density on a given lattice site—that is, doubly occupied sites (doublons) appear empty. For a two-spin mixture of fermions in the lowest band of the optical lattice, the parity-projected density is described by the magnetic moment operator (21) $\hat{m}_{z,i}^2 = \left(\hat{n}_{\uparrow,i} - \hat{n}_{\downarrow,i}\right)^2$, where $\hat{n}_{\sigma,i} = \hat{c}_{\sigma,i}^\dagger \hat{c}_{\sigma,i}$ is the number operator and $\hat{c}_{\sigma,i}$ ($\hat{c}_{\sigma,i}^\dagger$) are fermion annihilation (creation) operators for spin $\sigma = \uparrow, \downarrow$ on site i. Many repeated measurements yield the average local moment on each site (Fig. 1, A and D), which is a thermodynamic quantity that quantifies the interaction energy. This is evident when one rewrites the interaction energy term $U\hat{n}_{\uparrow,i}\hat{n}_{\downarrow,i}$ as $\frac{U}{2}(\hat{n}_{\uparrow,i} + \hat{n}_{\downarrow,i} - \hat{m}_{z,i}^2)$. The Fermi-Hubbard Hamiltonian can be written in terms of local moments as

$$\hat{H} = -t\sum_{\langle i,j \rangle, \sigma}(\hat{c}_{\sigma,i}^\dagger \hat{c}_{\sigma,j} + \text{h.c.}) - \frac{U}{2}\sum_i \hat{m}_{z,i}^2 - \mu\sum_i(\hat{n}_{\uparrow,i} + \hat{n}_{\downarrow,i}) \quad (1)$$

which is a form that highlights the particle-hole symmetry of the Hamiltonian. Here, $\langle i,j \rangle$ denotes nearest-neighbor sites i and j, t is the nearest-neighbor hopping amplitude, U is the on-site interaction energy, and μ is the chemical potential. At moderate temperatures and depending on the fillings $n_i = \langle \hat{n}_{\uparrow,i} + \hat{n}_{\downarrow,i} \rangle$, this model can yield metallic, band insulating, or Mott insulating states. At half-filling ($n_i = 1$) and at temperatures below the superexchange scale $4t^2/U$, quasi-long-range antiferromagnetic correlations arise. For a fixed temperature, these correlations are expected to be maximal when $U \approx 8t$, where the interaction energy equals the single-particle bandwidth. Upon doping, a pseudogap phase emerges; at even lower temperatures, one expects a d-wave superconducting state (1). Although the superexchange scale is about a factor of 2 lower than the temperatures achieved here, site-resolved detection of short-range correlations should already reveal precursory signs of physics at this energy scale.

Figure 1A shows a typical measurement of the site-resolved average local magnetic moment from ~90 individual experimental realizations at U/t = 7.2(1). Atoms are confined in a radially symmetric trapping potential. Under the local density approximation, this results in a varying local chemical potential and, thus, a spatially varying filling n throughout the sample. We prepared samples where the maximum filling, which occurs in the center of the trap, lies above n = 1. From radially averaged profiles (Fig. 1D), the half-filling point is identified as the radial position where the moment reaches its maximum. This follows from the

particle-hole symmetry of the moment operator $\hat{m}_{z,i}^2$, a property that holds for all of its averages and cumulants (21).

Because the local moment satisfies the operator identity $(\hat{m}_{z,i}^2)^2 = \hat{m}_{z,i}^2$, fluctuations of the local moment do not yield additional information.
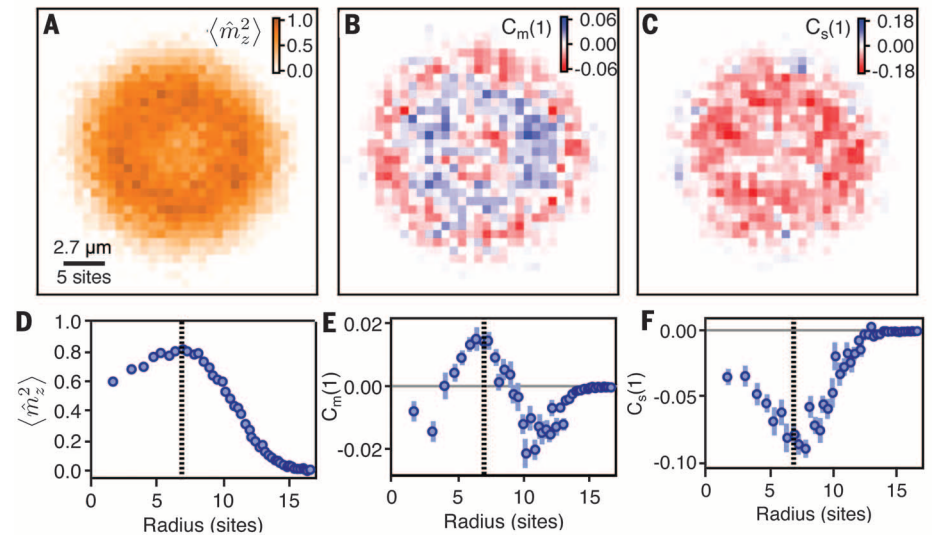

Fig. 1. Local moment and nearest-neighbor charge and spin correlations. An ultracold atom realization of the Fermi-Hubbard model for U/t = 7.2(1) is shown. (A to C) Local moment, nearest-neighbor moment correlator, and nearest-neighbor spin correlator, respectively, as functions of position, averaged over ~90 shots. The spatial variations reflect the varying local doping due to the underlying trapping potential. (D to F) Radial averages of (A), (B), and (C), respectively. The half-filling point is marked by vertical dotted lines.
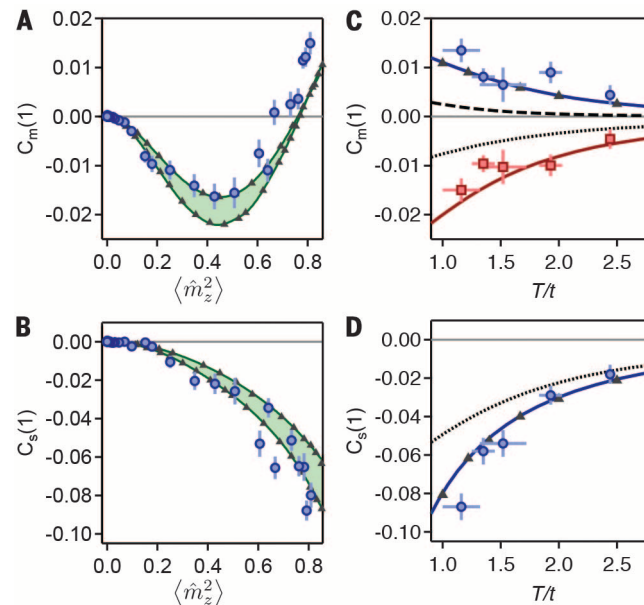

Fig. 2. Spin and moment correlators as functions of doping and temperature for U/t = 7.2(1). (A and B) Nearest-neighbor moment correlator [$C_m(1)$] (A) and spin correlator [$C_s(1)$] (B) as functions of the local moment, denoted by blue circles. Results from NLCE (and DQMC) for temperatures T/t = 0.89 and 1.22 are shown in green lines (and gray triangles), with the intermediate temperature range indicated by green shading. (C) The maximum and minimum of the moment correlator as functions of temperature are denoted by blue circles and red squares, respectively. Corresponding results are obtained from NLCE (solid blue line and solid red line, respectively), for the noninteracting gas (black dashed and dotted lines, respectively), and from DQMC for the correlator at half-filling (gray triangles). (D) Nearest-neighbor spin correlator at half-filling as a function of temperature (blue circles). Solid blue line, NLCE results; gray triangles, DQMC results; black dotted line, noninteracting gas. For all graphs, theory curves are not adjusted for the experimental imaging fidelity of 95%.

However, correlations of the moment between different sites do (27). We experimentally measured the moment correlator at a separation of one site, $C_m(1)$, defined as

$$C_m(1) = \frac{1}{4} \sum_{j \in nn_i} \left(\left\langle \hat{m}_{z,i}^2 \hat{m}_{z,j}^2 \right\rangle - \left\langle \hat{m}_{z,i}^2 \right\rangle \left\langle \hat{m}_{z,j}^2 \right\rangle \right)$$

(2)

where the sum is over all four nearest neighbors. The locally resolved correlator $C_m(1)$ at each site i and its radial average are shown in Fig. 1, B and E, respectively. $C_m(1)$ displays nonmonotonic behavior, changing sign as the filling is lowered.

The local moment correlator, however, is not sensitive to the sign of the spin $\hat{S}_{z,i} = \frac{1}{2}(\hat{n}_{\uparrow,i} - \hat{n}_{\downarrow,i})$. One important spin-sensitive correlator is $\langle \hat{S}_{z,i} \hat{S}_{z,j} \rangle$, which can reveal antiferromagnetic ordering, expected to occur at half-filling and at low temperatures. This correlator can be expressed as $\frac{1}{2}\sum_\sigma \langle \hat{p}_{\sigma,i} \hat{p}_{\sigma,j} \rangle - \frac{1}{4}\langle \hat{m}_{z,i}^2 \hat{m}_{z,j}^2 \rangle$ (28), where $\hat{p}_{\sigma,i} = \hat{n}_{\sigma,i} - \hat{n}_{\uparrow,i}\hat{n}_{\downarrow,i}$, which we measured by removing one spin state via resonant light, before imaging. All terms can be obtained experimentally in separate runs and are averaged separately. Analogous to the nearest-neighbor moment correlator $C_m(1)$, we define the nearest-neighbor spin correlator at site i

$$C_s(1) = \sum_{j \in nn_i} \left(\langle \hat{S}_{z,i} \hat{S}_{z,j} \rangle - \langle \hat{S}_{z,i} \rangle \langle \hat{S}_{z,j} \rangle \right)$$

(3)

Figure 1, C and F, show the locally resolved nearest-neighbor spin correlation $C_s(1)$ and its corresponding radial average, respectively. The fact that $C_s(1)$ is negative suggests antiferromagnetic correlations, as expected (29–31). However, even without interactions, Pauli-blocking of like spins suppresses $C_s(1)$. One can see this by noting

that $C_s(1)$ contains density correlations of either spin species separately $\left[\langle \hat{n}_{\sigma,i} \hat{n}_{\sigma,j} \rangle - \langle \hat{n}_{\sigma,i} \rangle^2 \right]$, which are negative even for the noninteracting gas thanks to Pauli suppression. For the lowest temperatures reached, we observed a maximum absolute spin correlation of about a factor of 2 larger than that of a noninteracting Fermi gas.

Figure 2, A and B, show the nearest-neighbor moment and spin correlations versus the measured local moment $\langle \hat{m}_{z,i}^2 \rangle$. This representation allows for comparison with theory under minimal assumptions. As a thermodynamic quantity, the moment can replace the role of the chemical potential μ. All thermodynamic variables can then be viewed as functions of the local moment, the spin correlation at half-filling, U, and t. In fact, the local spin correlation at half-filling is itself a thermometer that does not require any fit (32). Also shown in Fig. 2, A and B, are numerical linked-cluster expansion (NLCE) (33) and determinantal quantum Monte Carlo (DQMC) (34) calculations (28), which display similar behavior as the experimental data. Note that there are no free parameters; the temperature $T/t = 1.16(16)$ is obtained from the spin correlation at half-filling.

As expected, the antiferromagnetic spin correlations are maximum at half-filling and decrease in absolute value with increased doping. Moment correlations instead are negative at low to intermediate fillings, crossing zero around a moment of 0.75 (doping ≈0.21) before turning positive toward half-filling. This implies that moments change their character from effectively repulsive (antibunching) to effectively attractive (bunching). The antibunching and bunching behaviors in the moments, as well as the antiferromagnetic spin correlations, become more pronounced as the temperature is lowered. Figure 2C shows the moment

correlation at half-filling (maximum positive value), as well as its minimum value versus temperature. The spin correlator at half-filling (minimum value) (Fig. 2D) displays a similar temperature dependence, reaching –0.09 at the lowest temperatures in our experiment. This is about 30% of the maximum spin correlation expected for the spin-½ Heisenberg model at zero temperature in two dimensions (35).

To interpret the moment correlations, one may recast them in terms of the two-point correlator

$$g_2(r) = \frac{\langle \hat{m}_z^2(r) \hat{m}_z^2(0) \rangle}{\langle \hat{m}_z^2(r) \rangle \langle \hat{m}_z^2(0) \rangle}$$

(4)

which measures the probability of finding two moments a distance r from each other. In the absence of correlations, $g_2 = 1$. At low filling, for which the doublon density is negligible and the moment $\langle \hat{m}_z^2 \rangle = \langle \hat{n} \rangle - 2\langle \hat{n}_\uparrow \hat{n}_\downarrow \rangle \approx n$ is essentially the density, $g_2(r)$ measures density correlations. These are nontrivial even for the spin-polarized noninteracting Fermi gas, where fermion statistics lead to anticorrelations at short distances, reflecting the fact that two fermions cannot occupy the same site. This leads to Pauli suppression of g_2 that persists to a distance on the order of the average interparticle spacing, a feature known as the Pauli hole. Although implications of this fermion antibunching have been observed in the suppression of density fluctuations (36, 37) and momentum space correlations (38, 39), the real space suppression $g_2(r)$ has not been observed in situ before. In a noninteracting two-spin mixture, the anticorrelations are halved, as only two identical fermions experience the Pauli hole. However, repulsive interactions between opposite spins also suppress $g_2(r)$, leading to a combined Pauli and correlation hole.

In Fig. 3A, we show the directly measured $g_2(1)$ as a function of moment at an intermediate interaction of $U/t = 7.2$. The strong suppression of $g_2(1)$ at low fillings (large interparticle spacing) is observed and is stronger than Pauli suppression alone, reflecting short-range anticorrelations due to repulsive interactions. The data are well described by NLCE and DQMC calculations (Fig. 3A).

Whereas $g_2(r)$ measures the probability of finding two moments a distance r from each other, near half-filling, where $\langle \hat{m}_z^2 \rangle \sim 1$, the correlations arise mainly from sites where the moment is zero (i.e., sites with holes and doublons). The number of holes and doublons, which appear empty after imaging, is given by $\langle 1 - \hat{m}_z^2 \rangle$. The corresponding two-point correlation function $\bar{g}_2(r)$ of these anti-moments is thus

$$\bar{g}_2(r) = \frac{\langle (1 - \hat{m}_z^2(r))(1 - \hat{m}_z^2(0)) \rangle}{\langle 1 - \hat{m}_z^2(r) \rangle \langle 1 - \hat{m}_z^2(0) \rangle}$$

(5)

In Fig. 3B, we show that $\bar{g}_2(1)$ is strongly enhanced near half-filling beyond the uncorrelated value of 1. $\bar{g}_2(1)$ thus reveals the strong bunching of holes and doublons. There are three contributions
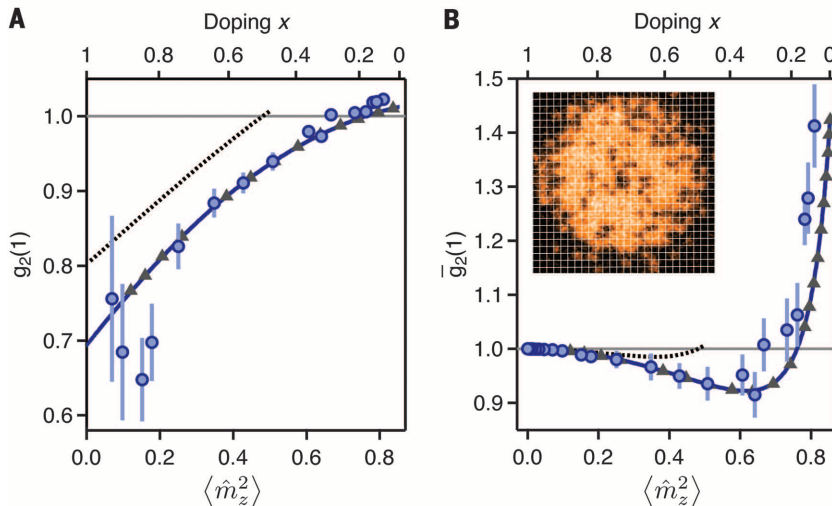

Fig. 3. Two-point correlation functions. g_2 is the correlation function for moments and $\bar{g}_2$ for antimoments at a separation of one lattice site for $U/t = 7.2(1)$. (**A**) $g_2(1)$ for moments. (**B**) $\bar{g}_2(1)$ for antimoments. Blue circles, experimental data; blue solid line, NLCE theory; gray triangles, DQMC theory. Both NLCE and DQMC calculations are performed at $T/t = 1.22$, and neither are adjusted for the experimental imaging fidelity of 95%. Black dotted lines, noninteracting gas. The doping x as a function of local moment is determined from NLCE theory at $T/t = 1.22$, without adjustment for imaging fidelity. (Inset) Typical image showing neighboring antimoments (imaged holes) near half-filling.

Fig. 4. Spin and moment correlations as functions of distance and doping.

(A) Moment and spin correlations for $U/t = 7.2(1)$ are shown in the top and bottom rows, respectively, at various values of the local moment. Correlation values are averaged over symmetric points. The moment correlator $C_m(0,1)$ changes sign near a local moment of $\hat{m}_z^2 \approx 0.75$. The anticorrelation of spins $C_s(0,1)$ is observed to weaken upon increasing doping (decreasing moment). In contrast, the next-nearest-neighbor spin correlator $C_s(1,1)$ changes from positive at zero doping to negative at large doping. (B) Moment and spin correlations obtained from DQMC theory for $U/t = 7.2(1)$ and $T/t = 1.00$ are shown in the top and bottom rows, respectively, at various values of doping x. The nonzero value of the moment and spin correlators at distance $(i,j) = (0,0)$ are omitted for clarity. They are both local quantities determined by the value of the moment. NLCE and DQMC results for the correlators at all distances shown are in good agreement (28).
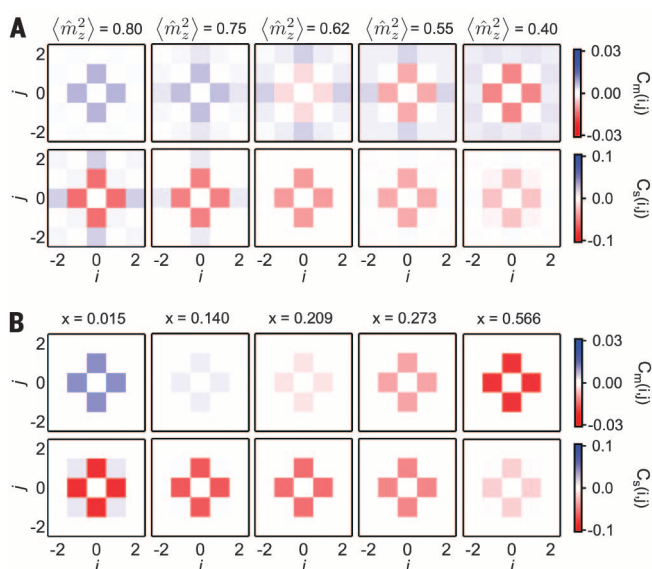
to $\bar{g}_2(1)$: correlations between pairs of holes, between pairs of doublons, and between holes and doublons. One expects neighboring holes and neighboring doublons to show negative correlations due to Pauli suppression and strong repulsion. Hence, the bunching behavior must originate from positive correlations between neighboring doublon-hole pairs. This expectation is confirmed by NLCE and DQMC calculations (28).

The strong doublon-hole correlation near half-filling in the presence of antiferromagnetic correlations can be qualitatively captured by a simple two-site Hubbard model, experimentally realized in (40). In the strongly interacting limit ($U \gg t$), the doublon density vanishes and the ground state is a spin singlet. However, at intermediate interaction strengths, tunneling admixes a doublon-hole pair into the ground state wave function, with an amplitude ~t/U. Thus, short-range singlet correlations at moderate U/t occur naturally together with nearest-neighbor doublon-hole correlations.

At a separation of one lattice site, we have revealed the competition between the combined Pauli- and interaction-driven repulsion of singly occupied sites and the effective attraction of doublons and holes, which manifests itself in a sign change of the correlator. The ability of the microscope to measure at a site-resolved level also allows investigation of longer-distance correlations. In Fig. 4, A and B, we show the moment and spin correlations $C_m(i,j)$ and $C_s(i,j)$, respectively, as a function of separation distance $i\hat{x} + j\hat{y}$. Near half-filling, even at the temperatures of this graph ($T/t \approx 1.2$), antiferromagnetic spin correlations beyond the next neighbor are visible. With increased doping, they give way to a more isotro-

pic negative spin correlation. For example, $C_s(1,1)$ changes sign from positive at half-filling to negative at large dopings. This resembles the effect of Pauli suppression that is already present for noninteracting fermions. For the moment correlator, we clearly observe the sign change of $C_m(1,0)$ at a doping of $x \approx 0.21$ and that the correlations do not extend substantially beyond one site.

The measurement of nonlocal moment correlations also results in direct access to the associated potential energy fluctuations (ΔE_{pot}). From the Fermi-Hubbard Hamiltonian in Eq. 1, we find that

$$\Delta E_{pot}^2 = \frac{1}{4} U^2 \left(\langle \hat{M}^2 \rangle - \langle \hat{M} \rangle^2 \right)$$
$$= \frac{1}{4} U^2 \sum_{i,j} \left(\langle \hat{m}_{z,i}^2 \hat{m}_{z,j}^2 \rangle - \langle \hat{m}_{z,i}^2 \rangle \langle m_{z,j}^2 \rangle \right)$$

$$(6)$$

where $\hat{M} = \sum_i \hat{m}_{z,i}^2$ is the total moment operator. At half-filling, the contribution to the fluctuations from the nearest-neighbor moment correlations is thus $U^2 C_m(1) \approx 0.8t^2$ for $T/t \approx 1$ and $U/t = 7.2(1)$. This suggests that doublon-hole correlations can arise from coherent tunneling of particles bound in spin singlets.

Away from half-filling, both NLCE and DQMC calculations are currently limited to a temperature range around $T/t \approx 0.5$, not far below what is reached experimentally in this work. Further reduction in experimental temperatures will provide a valuable benchmark for theoretical techniques, especially away from half-filling, where the sign problem arises. The clear importance of doublon-hole correlations will prompt further studies of their dynamics, especially away from

half-filling, which could elucidate their role for the transport properties of a possible strange metal phase and potential pseudogap behavior.

REFERENCES AND NOTES

1. P. A. Lee, N. Nagaosa, X.-G. Wen, *Rev. Mod. Phys.* **78**, 17–85 (2006).
2. P. W. Anderson, *Science* **235**, 1196–1198 (1987).
3. M. Inguscio, W. Ketterle, C. Salomon, Eds., *Ultracold Fermi Gases*, Proceedings of the International School of Physics "Enrico Fermi," Course CLXIV, Varenna, 20 to 30 June 2006 (IOS Press, 2008).
4. I. Bloch, J. Dalibard, W. Zwerger, *Rev. Mod. Phys.* **80**, 885–964 (2008).
5. T. Esslinger, *Annu. Rev. Condens. Matter Phys.* **1**, 129–152 (2010).
6. R. Jördens, N. Strohmaier, K. Günter, H. Moritz, T. Esslinger, *Nature* **455**, 204–207 (2008).
7. S. Taie, R. Yamazaki, S. Sugawa, Y. Takahashi, *Nat. Phys.* **8**, 825–830 (2012).
8. U. Schneider *et al.*, *Science* **322**, 1520–1525 (2008).
9. P. M. Duarte *et al.*, *Phys. Rev. Lett.* **114**, 070403 (2015).
10. D. Greif, T. Uehlinger, G. Jotzu, L. Tarruell, T. Esslinger, *Science* **340**, 1307–1310 (2013).
11. R. A. Hart *et al.*, *Nature* **519**, 211–214 (2015).
12. D. Greif, G. Jotzu, M. Messer, R. Desbuquois, T. Esslinger, *Phys. Rev. Lett.* **115**, 260401 (2015).
13. E. Cocchi *et al.*, *Phys. Rev. Lett.* **116**, 175301 (2016).
14. C. Hofrichter *et al.*, *Phys. Rev. X* **6**, 021030 (2016).
15. L. W. Cheuk *et al.*, *Phys. Rev. Lett.* **114**, 193001 (2015).
16. E. Haller *et al.*, *Nat. Phys.* **11**, 738–742 (2015).
17. M. F. Parsons *et al.*, *Phys. Rev. Lett.* **114**, 213002 (2015).
18. A. Omran *et al.*, *Phys. Rev. Lett.* **115**, 263001 (2015).
19. G. J. A. Edge *et al.*, *Phys. Rev. A* **92**, 063406 (2015).
20. D. Greif *et al.*, *Science* **351**, 953–957 (2016).
21. L. W. Cheuk *et al.*, *Phys. Rev. Lett.* **116**, 235301 (2016).
22. M. Endres *et al.*, *Science* **334**, 200–203 (2011).
23. M. Endres *et al.*, *Appl. Phys. B* **113**, 27–39 (2013).
24. R. Islam *et al.*, *Nature* **528**, 77–83 (2015).
25. M. Boll *et al.*, *Science* **353**, 1257–1260 (2016).
26. M. F. Parsons *et al.*, *Science* **353**, 1253–1256 (2016).
27. E. Kapit, E. Mueller, *Phys. Rev. A* **82**, 013644 (2010).
28. See the supplementary materials on *Science* Online.
29. J. E. Hirsch, *Phys. Rev. B* **31**, 4403–4419 (1985).
30. E. Khatami, M. Rigol, *Phys. Rev. A* **84**, 053611 (2011).
31. J. P. F. LeBlanc, E. Gull, *Phys. Rev. B* **88**, 155108 (2013).
32. M. J. H. Ku, A. T. Sommer, L. W. Cheuk, M. W. Zwierlein, *Science* **335**, 563–567 (2012).
33. M. Rigol, T. Bryant, R. R. P. Singh, *Phys. Rev. Lett.* **97**, 187202 (2006).
34. R. Blankenbecler, D. J. Scalapino, R. L. Sugar, *Phys. Rev. D Part. Fields* **24**, 2278–2286 (1981).
35. T. Paiva, R. Scalettar, M. Randeria, N. Trivedi, *Phys. Rev. Lett.* **104**, 066406 (2010).
36. C. Sanner *et al.*, *Phys. Rev. Lett.* **105**, 040402 (2010).
37. T. Müller *et al.*, *Phys. Rev. Lett.* **105**, 040401 (2010).
38. T. Rom *et al.*, *Nature* **444**, 733–736 (2006).
39. T. Jeltes *et al.*, *Nature* **445**, 402–405 (2007).
40. S. Murmann *et al.*, *Phys. Rev. Lett.* **114**, 080402 (2015).

POLYMER SCIENCE

Quantifying the impact of molecular defects on polymer network elasticity

Mingjiang Zhong,[1,2]* Rui Wang,[2]* Ken Kawamoto,[1]*
Bradley D. Olsen,[2]† Jeremiah A. Johnson[1]†

Elasticity, one of the most important properties of a soft material, is difficult to quantify in polymer networks because of the presence of topological molecular defects in these materials. Furthermore, the impact of these defects on bulk elasticity is unknown. We used rheology, disassembly spectrometry, and simulations to measure the shear elastic modulus and count the numbers of topological "loop" defects of various order in a series of polymer hydrogels, and then used these data to evaluate the classical phantom and affine network theories of elasticity. The results led to a real elastic network theory (RENT) that describes how loop defects affect bulk elasticity. Given knowledge of the loop fractions, RENT provides predictions of the shear elastic modulus that are consistent with experimental observations.

Molecular defects fundamentally govern the properties of all real materials (*1–3*). The language of crystallography has been successfully used to describe defects and to model their impact in materials with a degree of periodicity, such as silicon, steel, block copolymers, and liquid crystals. However, understanding defects in amorphous materials presents a continued challenge. In polymer networks, the relevant defects are largely of a topological nature: The properties of these amorphous materials depend primarily upon the way the molecules in the material are connected. Understanding the correlation between the network topology and properties is one of the greatest outstanding challenges in soft materials.

Polymer networks can have a wide range of shear elastic moduli (G') from ~10^2 to ~10^7 Pa (*4, 5*), with different applications requiring moduli across this entire range. Covalent polymer networks are generally formed via kinetically controlled processes; consequently, they possess cyclic topological defects. The classical affine and phantom network theories of network elasticity neglect the presence of such defects (*4, 5*); they rely on idealized end-linked networks (Fig. 1A) that consider only acyclic tree-like structures, which leads to overestimation of G' (*6, 7*). In practice, G' is frequently calculated according to the equation

$G' = Cv_{eff}kT$, where kT is the thermal energy, v_{eff} is the density of elastically effective chains, and C is a constant that has a value of 1 for the affine network model and $1 - 2/f$ for the phantom network model (where f is the functionality of the network junctions). Because polymer networks include elastically defective chains, v_{eff} is never known precisely, and thus neither theory is able to accurately fit experimental data; a controversy continues over which theory, if either, is correct. Thus, despite decades of advances in polymer network design, our inability to quantitatively calculate the effects of defects on shear elastic modulus and to measure the corresponding defect densities in real polymer networks precludes quantitative prediction of G' and validation of the affine and phantom network models (*4, 8–12*).

To understand how molecular structure affects G' and to use this knowledge to create a predictive theory of elasticity, it is first necessary to quantify the density of topological defects in a polymer network and to determine the impact of these defects on the mechanical properties of the network. Cyclic defects, created from intrajunction reactions during network formation, are chemically and spectroscopically almost identical to noncyclic junctions, making them difficult to distinguish and quantify (*5, 13–16*). We have developed symmetric isotopic labeling disassembly spectrometry (SILDaS) as a strategy to precisely count the number of primary loops (Fig. 1B), the simplest topological defects, in polymer networks formed from $A_2 + B_3$ and $A_2 + B_4$ reactions (*17–20*). Furthermore, we have developed Monte Carlo

simulations and kinetic rate theories that show that cyclic defects in these polymer networks are kinetically linked, such that experimental measurement of only the primary loops determines the densities of all higher-order defects including secondary (Fig. 1C) and ternary loops (Fig. 1D) (*21*). Here, we measured loop fractions and G' for a series of hydrogels, thus providing quantitative relationships between these parameters. With this information, we examined the classical affine and phantom network theories of elasticity, and we derived a modified phantom network theory—real elastic network theory (RENT)—that accounts for topological molecular defects.

To rigorously determine how molecular topological defects affect elasticity, it is necessary to measure the topological defect density and modulus in the same gel. A class of stable yet chemically degradable gels was developed from bis-azido-terminated polyethylene glycol (PEG) (number-average molecular weight M_n = 4600, dispersity index $Đ$ = 1.02) polymers with non-labeled or isotopically labeled segments near their chain ends, A_{2H} and A_{2D}, respectively (*22*) (structures are shown in Fig. 1A; for synthesis and characterization details, see figs. S1 to S3 and figs. S17 to S34). Such labeling provides a convenient method for precise measurement of primary loops by SILDaS (*19*). The PEG molecular weight ensures that the polymer solutions used to form gels are well below the entanglement regime (*5, 12*). The labeled (A_{2D}) and non-labeled (A_{2H}) polymers (referred to herein as "A_2 monomers") were mixed in a 1:1 molar ratio, and this mixture was allowed to react with a tris-alkyne (B_3) or a tetra-alkyne (B_4) (structures are shown in Fig. 1A) in propylene carbonate solvent to provide end-linked gels via copper-catalyzed azide-alkyne cycloaddition (*23, 24*). When the reactive group stoichiometry—azide and alkyne in this case—was carefully controlled to be 1:1, spectroscopic analysis demonstrated that dangling functionalities (unreacted azides or alkynes) could be minimized (*19*) such that their impact on elasticity is negligible. Gels with varied fractions of topological defects were synthesized by varying the initial concentrations of A_2 and B_3 or B_4 monomers (*22*).

For measurement of the shear elastic modulus as a function of gel preparation conditions, gel samples 1.59 mm thick were formed in situ in Teflon molds under an inert atmosphere (fig. S4). Gel disks (diameter 12 mm) were punched (Fig. 1A) and loaded onto an oscillatory shear rheometer equipped with parallel-plate geometry. Propylene carbonate was chosen as the solvent

[1]Department of Chemistry, Massachusetts Institute of Technology, Cambridge, MA 02139, USA. [2]Department of Chemical Engineering, Massachusetts Institute of Technology, Cambridge, MA 02139, USA.
*These authors contributed equally to this work. †Corresponding author. Email: bdolsen@mit.edu (B.D.O.); jaj2109@mit.edu (J.A.J.)

Science

Observation of spatial charge and spin correlations in the 2D Fermi-Hubbard model

Lawrence W. Cheuk, Matthew A. Nichols, Katherine R. Lawrence, Melih Okan, Hao Zhang, Ehsan Khatami, Nandini Trivedi,
Thereza Paiva, Marcos Rigol and Martin W. Zwierlein

ARTICLE TOOLS	http://science.sciencemag.org/content/353/6305/1260
SUPPLEMENTARY MATERIALS	http://science.sciencemag.org/content/suppl/2016/09/15/353.6305.1260.DC1
RELATED CONTENT	http://science.sciencemag.org/content/sci/353/6305/1253.full http://science.sciencemag.org/content/sci/353/6305/1257.full
REFERENCES	This article cites 43 articles, 7 of which you can access for free http://science.sciencemag.org/content/353/6305/1260#BIBL
PERMISSIONS	http://www.sciencemag.org/help/reprints-and-permissions

Use of this article is subject to the Terms of Service